ACS OMEGA

Open Access



http://pubs.acs.org/journal/acsodf

Article

# Excellent Gas-Sensitive Capabilities of $Co_3(HXTP)_2$ for Detecting Combustion Process Gases: A Theoretical Study

Tengrui Feng,[‖] Wanlin Xu,[‖] Degui Lin,[‖] Jiezhen Xia,* and Qi Wu*

Cite This: *ACS Omega* 2025, 10, 18380−18390

Read Online

ACCESS | Metrics & More | Article Recommendations | Supporting Information

**ABSTRACT:** Combustion processes produce noxious gases, causing environmental pollution and health risks, which require high-performance sensing materials. Herein, metal−organic framework structures (MOFs) $Co_3(HXTP)_2$ (X = H, I, T) with superior conductivity and sensing properties are employed based on density functional theory (DFT) calculations. Adsorption energies of $Co_3(HXTP)_2$@gas are exceptionally outstanding in the realm of gas-sensitive material. $Co_3(HXTP)_2$ bases exhibit a responsive behavior toward the gas by comparing the work function and have a short recovery time ($\tau$). Our results demonstrate that $Co_3(HHTP)_2$ ($\tau$ = 1.226 s) and $Co_3(HITP)_2$ ($\tau$ = 19.441 s) can serve as gas-sensitive materials for detecting $O_2$ at 298 K, whereas $Co_3(HTTP)_2$ ($\tau$ = 694.226 s) can be used for CO at 498 K. Moreover, excellent gas-sensitive properties arise from chemical interactions, such as the electron "donation−backdonation" mechanism between gas and substrate ($\sigma \rightarrow 3d_z^2$ and $3d_{xz}$, $3d_{yz} \rightarrow \pi^*$), and the simultaneous refilling of the d-suborbitals ($3d_z^2 \rightarrow 3d_{xz}$, $3d_{yz}$) within Co atoms. The descriptor $\varphi$ demonstrates excellent predictive capability for both the adsorption and response of gas-sensitive materials. Our findings provide valuable insights into the design of gas-sensitive materials in this class of $TM_3(HXTP)_2$ structures.

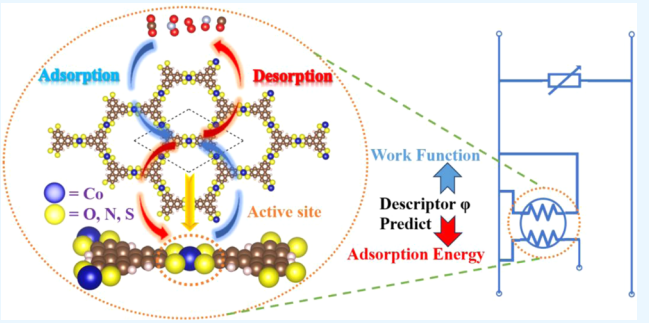


## INTRODUCTION

Gases in the combustion process (GCPs), including $O_2$, CO, $CO_2$, NO, and $NO_2$, are among the most common atmospheric components. Specifically, excessive $O_2$ intake can accelerate aging in humans. Combustion products such as NO and $NO_2$ contribute to acid rain and smog formation, leading to severe soil and water pollution. The presence of CO causes gas poisoning. $CO_2$ plays a prominent role in global greenhouse effects. Excessive inhalation of GCPs not only poses significant risks to human cognitive function but also jeopardizes life itself. Consequently, the accurate identification and quantification of these gases are of paramount importance for the surveillance of the ecological environment and the safeguarding of human health.

To accurately and quickly monitor the aforementioned gases, a great deal of studies have been conducted on various gas-sensitive materials,[1,2] including metal oxide,[3−5] carbon-based materials,[6−8] and transition metal dichalcogenides[9−12] (TMDs). However, these materials possess certain limitations to some extent. Due to the strong polarity of oxygen, metallic oxide materials exhibit robust adsorption against specific gases but require high temperatures for activation, thereby resulting in increased energy consumption and rendering them unsuitable for mobile devices. Carbon-based materials such as graphene lack polar active sites, leading to limited sensor sensitivity and selectivity. TMDs are effortless to degradation caused by adsorbed gases, leading to the irreversible depletion of raw materials. Due to the various defects in these materials, there is an urgent need to identify more suitable gas-sensing materials.

Metal−organic framework structures (MOFs) have a wide range of physical and chemical properties, such as the large specific surface area and high porosity, as well as a wealth of active sites due to their diverse combinations of polar atoms.[13−20] To date, the synthesis of MOFs can be realized through simple room-temperature preparation via a top-down solution process. The easily controllable and remarkably efficient catalytic activity bestows MOF materials with significant research and application value in the pharmaceutical and chemical industries. Nevertheless, most MOFs exhibit low electrical conductivity,[18,21] which significantly influences the performance of electrochemical gas sensors. Pentyala and his colleagues[16] found that the original MOF-74 has poor electrical conductivity. After functional modification with Mg and ethylene diamine, the material not only improved its electrical conductivity but also enhanced its sensing ability

Received: November 20, 2024
Revised: February 21, 2025
Accepted: April 11, 2025
Published: April 28, 2025

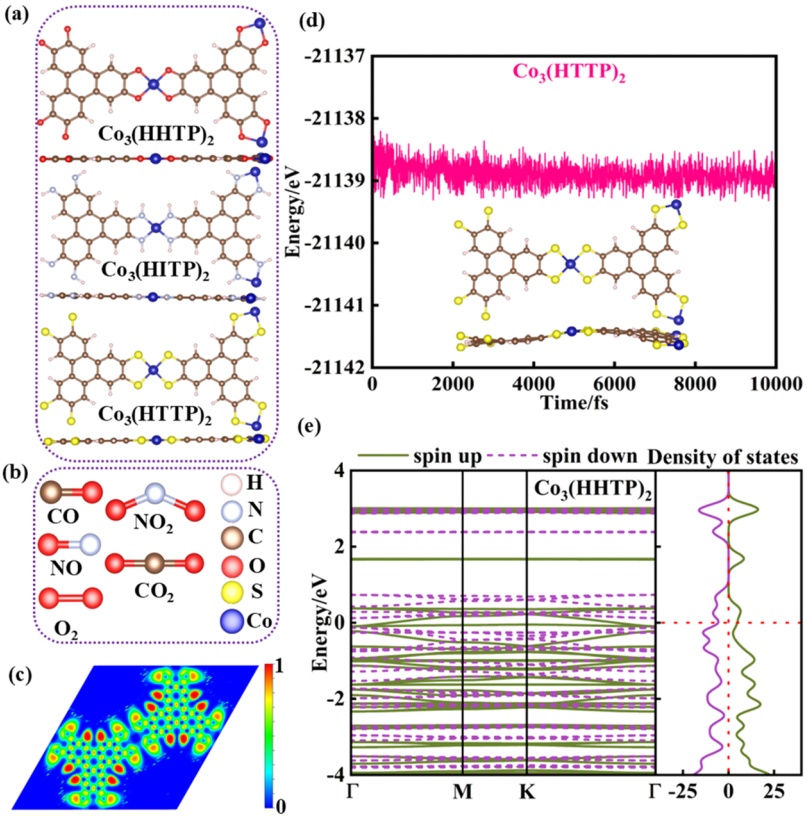


**Figure 1.** Optimized structure of (a) $Co_3(HXTP)_2$ and (b) GCP gases. (c) Calculated electron localization function (ELF) of $Co_3(HHTP)_2$. (d) AIMD simulation for $Co_3(HTTP)_2$ at 498 K. (e) Band structure and density of states for $Co_3(HHTP)_2$. The Fermi level is set to be zero (denoted as red dotted lines).

toward $CO_2$. As a result, it is interesting to find a MOF material with good electrical conductivity and explore its potential as a gas-sensitive material.

Recently, a novel MOF material $TM_3(HXTP)_2$ (X = H, I, T) has already been synthesized[22−33] and exhibited potential for room-temperature conductivity.[22−36] The single-layer $TM_3(HXTP)_2$ structure is predominantly constructed from metal atoms and organic ligands HITP ($C_{18}H_{12}N_6$), HHTP ($C_{18}H_6O_6$), and HTTP ($C_{18}H_6S_6$) interconnected through covalent bonds. The favorable energy matching between the linker and the metal orbitals facilitates the extension of the $\pi$-conjugated system, which promotes effective in-plane delocalization of charge carriers and endows outstanding electrical conductivity. Moreover, the periodic cavity with a size of approximately 22 Å theoretically enables the encapsulation of a greater number of gas molecules within superlarge pores.

$TM_3(HXTP)_2$ is widely used for its excellent electrocatalytic performance, but there are also some experiments in the field of gas-sensitive materials that confirm its superior gas-sensing properties. Yao et al.[28] reported that $Cu_3(HHTP)_2$ thin films exhibit outstanding room-temperature sensing performance for the selective detection of $NH_3$ with a rapid response time, excellent long-term stability, and reproducibility. Campbell et al.[37] successfully utilized $Cu_3(HHTP)_2$, $Cu_3(HITP)_2$, and $Ni_3(HITP)_2$ materials for the detection of volatile organic gases (VOCs), encompassing five functional groups such as alcohols, aromatics, ketones, amines, and alkanes. Despite all of these applications, the gas-sensing characteristics of $TM_3(HXTP)_2$ toward combustion process gases have never been investigated. Therefore, it is necessary to reveal the potential application of $TM_3(HXTP)_2$ (X = H, I, T) as a new kind of gas-sensitive material for GCPs.

In this study, taking advantage of the excellent electrical conductivity exhibited by $Co_3(HXTP)_2$,[27,30,31,33−35,38] we explore their feasibility as gas-sensitive materials for detecting GCPs. The gas-sensitive performance of these materials was evaluated through their adsorption, response, and desorption behaviors with respect to GCPs. To further elucidate the origins of their gas-sensing properties, we performed a detailed analysis of each material's electronic structures. Results indicate that $Co_3(HHTP)_2$ and $Co_3(HITP)_2$ are effective for detecting $O_2$, while CO adsorption exhibits favorable electronic and geometric characteristics on the $Co_3(HTTP)_2$ monolayer, suggesting its potential as a highly responsive material for gas-sensing applications. Furthermore, we developed a new descriptor $\varphi$ to quantify the response and adsorption properties of gas-sensitive materials. Our results can provide a theoretical basis for future experimental validation, thereby promoting the application of $Co_3(HXTP)_2$ materials in the detection of gases from combustion processes. This comprehensive investigation underscores the potential of $Co_3(HXTP)_2$-based materials for GCP gas detection and offers valuable insights into the application of $TM_3(HXTP)_2$ as an effective gas sensors.

## COMPUTATIONAL DETAILS AND METHODS

In this study, all of the first-principles spin-polarized calculations are performed using the Vienna Ab-initio Simulation Package[39] (VASP 5.4.4). The interaction between ions and electrons is described employing projector augmented


https://doi.org/10.1021/acsomega.4c10559
ACS Omega 2025, 10, 18380−18390

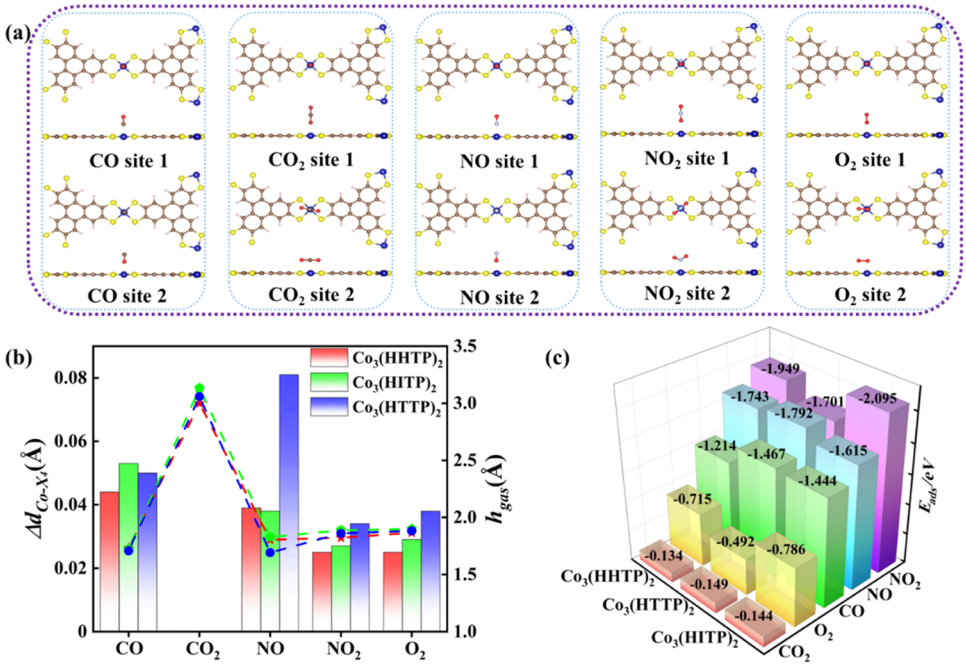


**Figure 2.** (a) Adsorption configurations of GCPs on $Co_3(HTTP)_2$. (b) Bar plot represents the change of the average bond length of the Co-$X_4$ center ($\Delta d_{Co\text{-}X_4}$) and the line plot shows the adsorption height ($h_{gas}$) of GCPs. (c) Adsorption energies of various adsorption systems.

waves[40] (PAW) pseudopotential, while the exchange-correlation potential is determined by utilizing the generalized gradient approximation (GGA) with the Perdew–Burke–Ernzerhof[41] (PBE) functional. The DFT-D3[42] correction of the Grimme scheme is employed to elucidate the van der Waals (vdW) interactions between the gases and substrates. The cutoff energy is set to 520 eV, while criteria of $10^{-5}$ eV and 0.02 eV/Å are employed for achieving force and energy convergence in the calculation. To eliminate the interaction brought by the periodic repeating units, a vacuum layer of 15 Å thickness is added in the z direction. The 2 × 2 × 1 and 3 × 3 × 1 k-point meshes generated based on the Monkhorst–Pack scheme were employed for the geometric optimization and calculation of the density of states (DOS) for all systems. Furthermore, the Bader charge analysis is employed to quantitatively analyze the charge transfer between the gas and the substrate. DS-PAW[43] 2023A software is utilized for ab-initio molecular dynamic[44] (AIMD) simulations to determine the thermodynamic stability of $Co_3(HTTP)_2$ simulated at 498 K for 10 ps. The initial placement of the gas is optimized by locating it 2 Å[7,45] away from the surface. The projected crystal orbital Hamilton populations (pCOHP) are calculated using the LOBSTER 4.1.0 procedure to quantitatively study the bond interaction between atoms.

To evaluate the capturing ability of $Co_3(HXTP)_2$, the adsorption energy between gas and substrate is calculated by the following formula:[9,46,47]

$$E_{ads} = E_{gas@Co_3(HXTP)_2} - E_{Co_3(HXTP)_2} - E_{gas} \quad (1)$$

where $E_{gas@Co_3(HXTP)_2}$, $E_{Co_3(HXTP)_2}$, and $E_{gas}$ represent the total energy of gas@$Co_3(HXTP)_2$ adsorption systems, the $Co_3(HXTP)_2$, and the adsorbed GCP gas, respectively.

The VESTA software is utilized for visualizing the charge density difference between the gas and the substrate using the subsequent formula:[3,6,7]

$$\Delta\rho = \rho_{gas@Co_3(HXTP)_2} - \rho_{Co_3(HXTP)_2} - \rho_{gas} \quad (2)$$

where $\rho_{gas@Co_3(HXTP)_2}$, $\rho_{Co_3(HXTP)_2}$, and $\rho_{gas}$ are the charge density of the adsorption systems, $Co_3(HXTP)_2$, and the adsorbed gas, respectively.

## RESULTS AND DISCUSSION

**Structures of GCPs and $Co_3(HXTP)_2$ (X = H, I, T).** For combustion process gases, which mainly contain $CO_2$, CO, $O_2$, NO, and $NO_2$, the optimized structure is shown in Figure 1b, and geometric structure information and physicochemical properties are listed in Table S1. It is noteworthy that $O_2$ exhibits a magnetic moment of 2 $\mu_B$, and NO and $NO_2$ possess a magnetic moment of 1 $\mu_B$. Additionally, calculations have been performed for the highest occupied orbital (HOMO) and lowest unoccupied orbital (LUMO) of GCPs, which are presented in Table S1. The HOMO and LUMO band gaps ($E_{L\text{-}H}$) can serve as an indicator of their electron-donating and feedback capabilities to a certain extent. The $E_{L\text{-}H}$ width of GCPs follows the order as $CO_2$ (8.108 eV) > CO (6.886 eV) and $O_2$ (6.759 eV) > NO (4.383 eV) > $NO_2$(2.855 eV), suggesting a potential adsorption energy sequence of $CO_2$ < CO and $O_2$ < NO < $NO_2$.

$Co_3(HXTP)_2$ (X = H, I, T) can be categorized into three types, designated as $Co_3(HHTP)_2$, $Co_3(HITP)_2$, and $Co_3(HTTP)_2$, which, respectively, correspond to X ligand atoms containing O, N, and S. The $Co_3(HXTP)_2$ structures are relaxed, as depicted in Figure 1a, consistent with the early reports.[34,35,38] The calculated lattice parameters for $Co_3(HHTP)_2$ are $a = b = 21.50$ Å, the average bond lengths of Co-$X_4$ ($d_{Co\text{-}X4}$) center are 1.83 Å, and the magnetic moment ($M$) are 3.206 $\mu_B$. In addition, the electron localization function (ELF) diagram in Figure 1c illustrates the formulation of the electron cavity for $Co_3(HHTP)_2$ around the Co-$X_4$ center, primarily originating from the unbonded electron pairs of the X ligand atoms, which facilitate gas molecule adsorption


https://doi.org/10.1021/acsomega.4c10559
ACS Omega 2025, 10, 18380−18390

and thus are selected as potential adsorption sites. The calculated band structures and density of states (DOS) of $Co_3(HHTP)_2$ are presented in Figure 1e and Table S2. $Co_3(HHTP)_2$ possesses an almost negligible band gap ($E_g$) width of approximately 0.017 eV. The calculated lattice parameters for $Co_3(HITP)_2$ are $a = b = 21.91$ Å, the $d_{Co\text{-}X4}$ is 1.83 Å, and the $M$ is 3.067 $\mu_B$. The ELF diagram is presented in Figure S1a, and band structures and DOS are presented in Figure S3. $Co_3(HITP)_2$ exhibits semiconductor behavior with band gap widths of 0.212 eV. Lattice parameters for $Co_3(HTTP)_2$ are $a = b = 23.22$ Å, the $d_{Co\text{-}X4}$ is 2.13 Å, and the $M$ is 2.823 $\mu_B$. Figure S1b is the ELF diagram, and band structures and DOS are presented in Figure S4 with $E_g$ widths of 0.399 eV. Moreover, ab-initio molecular dynamic (AIMD) simulation was performed to determine the stability of $Co_3(HTTP)_2$. As depicted in Figure 1d, $Co_3(HTTP)_2$ can well maintain the structural integrity after 10 ps at the high temperature of 498 K, exhibiting remarkable thermodynamic stability. In summary, all $Co_3(HXTP)_2$ substrates demonstrate remarkable stability and excellent electrical conductivity.

**Adsorption Behaviors of $Co_3(HXTP)_2$ (X = H, I, T) on the GCPs.** Two adsorption manners were considered in order to evaluate the adsorption behaviors for GCPs, as seen in Figure 2a. NO and CO molecules are adsorbed on the $Co_3(HXTP)_2$ surface with the O-terminal (site 2) or N, C-terminal (site 1). $CO_2$, $NO_2$, and the $O_2$ molecules are placed vertically to the substrate surface end with the O atom (site 1) or horizontally (site 2) to the substrate. The optimized structures can be found in Figure S5. It can be seen that upon CO/NO adsorption, the gas molecule can be perpendicular to the monolayer or inclined adsorbed with the C or N atoms pointing to the Co adatom. For the $O_2$ and $NO_2$, they prefer to be inclined adsorbed on the surface accompanied by O binding with the Co adatom. The average bond length of the Co-X center ($d_{Co\text{-}X_4}$), and the adsorption height of GCPs ($h_{gas}$) can be found in Table S3. For the Co-$X_4$ center, the calculated difference of the average bond length of the Co-X center ($\Delta d_{Co\text{-}X_4}$) ranges from 0.025 to 0.081 Å (see Figure 2b), manifesting that the Co atom is slightly pulled out of the $Co_3(HXTP)_2$ plane upon GCPs adsorption. The summarized absorption energies ($E_{ads}$) of $Co_3(HXTP)_2$ to each GCP gases as illustrated in Figure 2c show that the $Co_3(HXTP)_2$ has strong chemisorption for CO, NO, and $NO_2$, with $E_{ads}$ ranging from −1.214 to −2.095 eV. And the adsorption energy of GCPs gases exhibits a strong inverse ratio with their $E_{L-H}$, as previously speculated. The large $E_{ads}$ for GCPs are associated with the newly forming Co−O/C/N bonds ($l_{Co\text{-}gas}$) in Table S4 (ranging from 1.679 to 1.903 Å), which also indicate the strong interaction. In contrast, the $O_2$ molecule possesses a medium adsorption energy (−0.492 to −0.786 eV) on the $Co_3(HXTP)_2$. The $CO_2$ adsorption systems with $E_{ads}$ values of −0.134 to −0.149 eV exhibit much weaker interactions and a physical adsorption nature, indicating that the substrate does not provide sufficient anchoring for $CO_2$. Therefore, it should be excluded from consideration for the next studies. Furthermore, the strong interaction between $NO_2$ and the substrate may surpass our expectations, thereby posing a challenge for desorption. Compared with other common gas-sensitive materials, it can be found that the adsorption energy values of $Co_3(HXTP)_2$ for CO/NO/$NO_2$/$O_2$ exceed those reported in previous studies as listed in Table 1. The adsorption of GCP gases on two-dimensional surfaces such as $MoS_2$, $BC_3$, and $As_2C_3$ is relatively limited. In contrast, the superior adsorption energy of $Co_3(HXTP)_2$ can be primarily attributed to its unique charge cavity, which facilitates gas adsorption and enhances chemical interactions with metal atoms. Moreover, our results surpass those achieved through engineering modifications, such as doping or defect introduction, as reported in previous studies. In summary, compared to other two-dimensional surfaces, $Co_3(HXTP)_2$ has a more outstanding gas-anchoring ability. The strong adsorption energy is primarily due to the stronger adsorption of gas molecules by the electron cavity, leading to more intense electron-transfer-dominated chemical interactions. Thus, the adsorption behavior analysis shows the practical application of $Co_3(HXTP)_2$ sheet as a potential gas sensor.

**Table 1. Comparison of the Adsorption Energies of $Co_3(HTTP)_2$@CO/NO/$NO_2$/$O_2$ in This Study and in Previous Studies**

| systems | $E_{ads}$, eV | systems | $E_{ads}$, eV |
|---|---|---|---|
| $Co_3(HTTP)_2$@CO (this work) | −1.467 | $Co_3(HITP)_2$@$NO_2$ (this work) | −2.095 |
| Ag-$PdSe_2$@CO[46] | −0.714 | $MoS_2$@$NO_2$[9] | −1.57 |
| Ga-graphene@CO[7] | −0.674 | $BC_3$@$NO_2$[48] | −1.69 |
| Ag-Bi@CO[49] | −1.42 | GeBi@$NO_2$[50] | −1.09 |
| 2D-Mg@CO[45] | −0.508 | Au-BSe@$NO_2$[51] | −1.12 |
| $Co_3(HTTP)_2$@NO (this work) | −1.792 | $Co_3(HITP)_2$@$O_2$ (this work) | −0.786 |
| In-$Ti_2O$@NO[3] | −0.91 | $Fe_2GeS_4$(010)@$O_2$[52] | −0.46 |
| $As_2C_3$@NO[53] | −0.31 | $V_3S_4$@$O_2$[54] | −0.59 |
| $C_{3.6}B$@NO[55] | −0.57 | N-graphene@$O_2$[56] | −0.123 |
| Sb-$MoTe_2$@NO[57] | −0.74 | bilayer $TiS_2$@$O_2$[58] | −0.086 |

**Intrinsic Mechanism of the Adsorption.** The origin of these strong adsorption energies has been elucidated through a deeper-order intrinsic mechanism analysis. Taking $Co_3(HTTP)_2$@CO as an example, the spin-polarized total density of states (TDOS) and projected density of states (PDOS) are provided in Figure 3a,b, while Figure S6 displays TDOS for other adsorption systems. Figure 3a clearly demonstrates that the introduction of gas induces a shift in the overall energy levels toward higher energy positions, which can be potentially attributed to the electron flow directed from the substrate to the gas.

The first row in Figure 3b shows four characteristic orbitals, namely, 4$\sigma$*, 1$\pi$, 5$\sigma$, and 2$\pi$* in free CO molecular within the range of −6 to 6 eV. The 5$\sigma$ orbital, being in close proximity to the Fermi energy level, exhibits a higher tendency for electron donation, whereas the 2$\pi$* orbital, positioned above the Fermi level, is more inclined toward accepting electrons. As shown in lines 2 to 3 in Figure 3b, the electrons were obviously transferred from the 5$\sigma$ orbital of CO to the $3d_z^2$ orbitals of Co after CO adsorption. Correspondingly, the unoccupied $d$ orbitals of the Co atom accepted the electrons from *CO, forming the Co−C bonding state to strengthen the CO capture, as evidenced by the evident hybridization between Co_3d and C_2p orbitals around the Fermi level.[59] The integral value of the COHP (ICOHP) between the Co_3d orbital and the C_2p orbital is −1.89 eV, confirming the formation of a chemical bond. Furthermore, both $3d_{xz}$ and $3d_{yz}$ orbitals experience splitting, leading to the occupation states spanning a broader energy range above and below the Fermi level, accompanied by the disappearance of the asymmetrical peaks. It illustrates that electrons are returned to the hollow antibonding 2$\pi$* orbital of the gas by metal $d_{xz}$ and $d_{yz}$ orbitals,


https://doi.org/10.1021/acsomega.4c10559
ACS Omega 2025, 10, 18380−18390

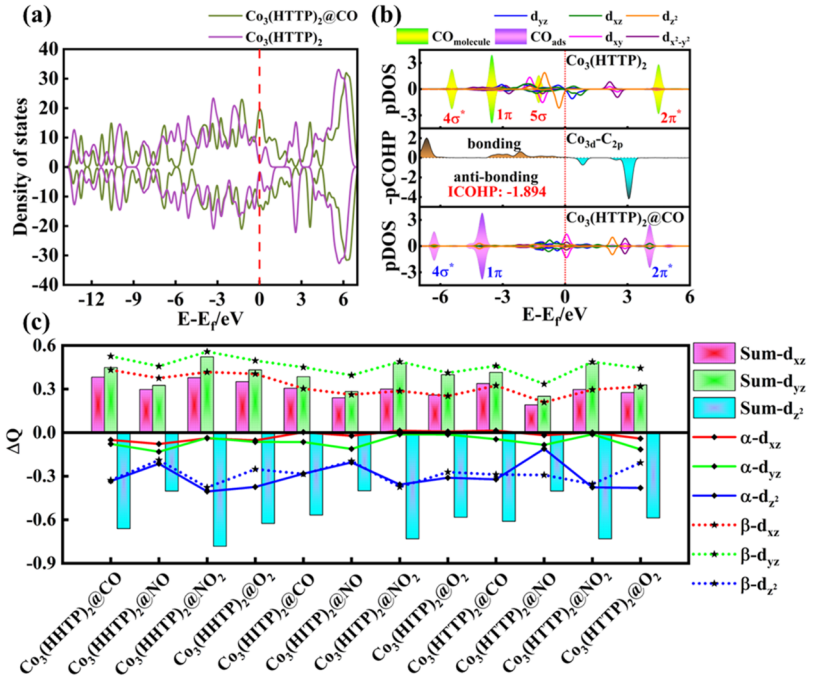


**Figure 3.** (a) TDOS spectra of $Co_3(HTTP)_2$ and $Co_3(HTTP)_2$@CO. (b) PDOS of Co_3d and the TDOS of CO molecules before adsorption, the COHP and ICOHP for the Co_3d orbital and C_2p orbital, the PDOS of Co_3d and CO molecules after adsorption. (c) Disparity in the number of electrons between $\alpha$-$d_{xz}$, $\beta$-$d_{xz}$, $\alpha$-$d_{yz}$, $\beta$-$d_{yz}$, $\alpha$-$d_{z^2}$, and $\beta$-$d_{z^2}$ orbitals, and the total number of electron changes for $3d_{xz}$ (Sum-$d_{xz}$), $3d_{yz}$ (Sum-$d_{yz}$), and $3d_{z^2}$ (Sum-$d_{z^2}$) orbitals.

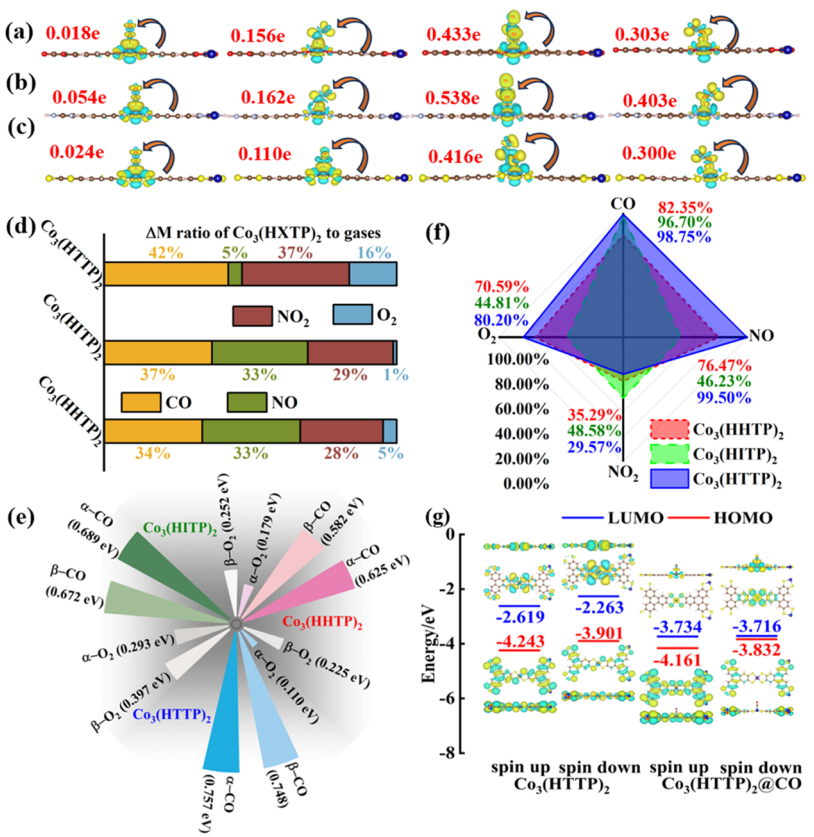


**Figure 4.** (a–c) Charge density differences of CO, NO, $NO_2$, and $O_2$ adsorbed on $Co_3(HXTP)_2$ (X = H, I, T). Iso-surfaces is set to 0.01 e/Bohr$^3$. (d) Percentage of changes in magnetic moments for different gases on $Co_3(HXTP)_2$ (X = H, I, T). (e) $E_{gap}$ of both spin-up ($\alpha$) and spin-down ($\beta$) orbitals in all $O_2$ and CO adsorption systems. (f) Change rate of band gap changes. (g) Schematic representation of the spin-polarized HOMO and LUMO orbit for $Co_3(HTTP)_2$ and $Co_3(HTTP)_2$@CO.



https://doi.org/10.1021/acsomega.4c10559
ACS Omega 2025, 10, 18380−18390

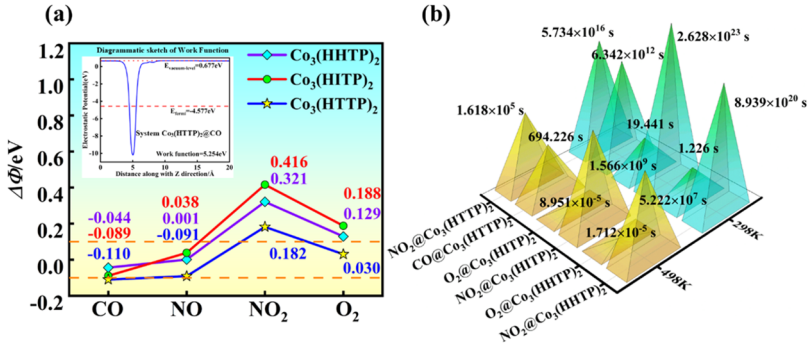


**Figure 5.** (a) Schematic of the work function for $Co_3(HTTP)_2$@CO and the changes in the work function (ΔΦ). The orange line represents ΔΦ of ± 0.1 eV. (b) $\tau$ of the adsorption systems.

following the mechanism of "donation−backdonation". As a result, $2\pi^*$ orbitals of adsorbed *CO on the catalyst reveal a significant downshift in comparison with isolated CO molecular. In summary, there exists a "donation−backdonation" electron exchange mechanism between the Co atom at the adsorption site and the vertically adsorbed gas molecule. Specifically, the gas molecule donates electrons from its highest occupied $\sigma$ orbital to the metal $d_z^2$ orbital, which satisfies the orbital symmetry and has a similar energy level. In return, the metal $d_{xz}$ and $d_{yz}$ orbitals backdonate a portion of electrons to the lowest unoccupied $\pi$ orbital of the gas molecule.

In addition, we also quantitatively analyze the electron number ($Q_d$) and disparity in the number ($\Delta Q_d$) of 3d orbitals of Co before and after adsorption by integrating PDOS into the Fermi level, as shown in Tables S5 and S6. It can be seen that the $3d_z^2$ orbital undergoes electron loss, while the $3d_{xz}$ and $3d_{yz}$ orbitals experience electron gain, as seen in Figure 3c. Furthermore, the accepted electrons are found in the spin-down $3d_{xz}$ ($\beta$-$d_{xz}$) and $3d_{yz}$ ($\beta$-$d_{yz}$) orbitals, whereas the lost electrons occupy the spin-up and spin-down $3d_z^2$ orbitals ($\alpha$-$d_z^2$ and $\beta$-$d_z^2$). Hence, the electron-transfer behavior is not limited to a simple $5\sigma \rightarrow 3d_z^2$ and $3d_{xz}$, $3d_{yz} \rightarrow 2\pi^*$ transition. Instead, the electrons obtained in $3d_z^2$ from the $5\sigma$ orbital are refilled into the $3d_{xz}$ and $3d_{yz}$ orbitals ($3d_z^2 \rightarrow 3d_{xz}$, $3d_{yz}$) where the electrons were previously depleted. Moreover, the electrons in the $3d_{x^2-y^2}$ and $3d_{xy}$ orbitals remain the same, demonstrating their presence in the adsorption system as nonbonding orbitals.

Furthermore, the amount of Bader charge transfer between GCPs and $Co_3(HXTP)_2$ (X = H, I, T) was analyzed based on the simulation of charge density differences (CDD). The yellow region represents the charge accumulation, and the cyan color is the region of charge depletion in Figure 4a−c. As shown in Figure 4a−c, the GCP molecules gained simultaneously in the hollow region of the $Co_3(HXTP)_2$ surface, which indicated that the charges of GCPs are transformed to the nanosheet. The Bader charge analysis shows 0.3−0.403 and 0.416−0.538 e charge transfer for $O_2$ and $NO_2$, which is a very high amount than other GCP molecules.

The magnetic moments ($M$) of both the gas and substrate warrant our attention. The density profiles of spin-polarized electron states can be observed in Figure S7. In comparison to the pristine $Co_3(HXTP)_2$ substrate, CO adsorption leads to a complete disappearance of spin-polarized electrons at the adsorption site, whereas $O_2$ adsorption preserves these spin-polarized electrons. Specifically, the percentage change in the magnetic moment ($\Delta M$%) caused by the adsorption of each gas on substrates $Co_3(HTTP)_2$, $Co_3(HITP)_2$, and $Co_3(HHTP)_2$, as seen in Figure 4d, is calculated by

$$\Delta M\% = \frac{\Delta M_i^{slab}}{\sum_i \Delta M_i^{slab}}\% \quad (3)$$

where $\Delta M_i^{slab}$ is the magnetic moment change caused by the adsorption of gas i (CO, NO, $NO_2$, and $O_2$) on base slab $Co_3(HXTP)_2$ (X = H, I, and T). The CO adsorption system shows the largest $\Delta M$%, whereas the $\Delta M$% for the $O_2$ adsorption system remains comparatively low, showing two distinct differences in the changes of magnetic moments ($\Delta M$, as provided in Table S7). Meanwhile, $M_{gas+surface}$ (after gas adsorption) undergoes a certain decrease compared to that of $M_{surface}$ (pristine surface), except for $Co_3(HITP)_2$@$O_2$. As shown in Figure 4e, we use the maximum energy gap between the 3d suborbital band centers ($E_{gap}$) to roughly evaluate the trend in magnetic moment changes; a higher $E_{gap}$ corresponds to a more pronounced $\Delta M$. Obviously, the $E_{gap}$ for CO adsorption (0.582−0.757 eV) is consistently higher than that for $O_2$ adsorption (0.110−0.397 eV) across all substrates, leading to a significantly greater $\Delta M$ in the CO system compared to the $O_2$ system.

The conductivity of the $Co_3(HXTP)_2$@GCPs (X = H, I, T) can be estimated based on the band gap ($E_g$) as shown in the following equation:[45,60,61]

$$\sigma \propto \exp\left(\frac{-E_g}{2k_B T}\right) \quad (4)$$

Additionally, the change rate of the band gap ($\Delta E_g$ %) is also calculated as follows:

$$\Delta E_g\% = \frac{|\Delta E_g|}{E_{gs}} \quad (5)$$

where $\Delta E_g = E_{ga} - E_{gs}$ is the band gap difference of the adsorption systems ($E_{ga}$) and the pristine $Co_3(HXTP)_2$ (X = H, I, T) slab ($E_{gs}$), the $T$ denotes temperature, and the $k_B$ is Boltzmann's constant ($8.62 \times 10^{-5}$ eV $K^{-1}$). As shown in Table S4, the band gaps all decreased with different degrees with the values of $\Delta E_g$ in the range of −0.006 to −0.397 eV. The conductivity of the substrate dramatically improves along with the reduction of band gap in all adsorption systems, which is advantageous for detecting resistance changes caused by gas adsorption. Specifically, $\Delta E_g$ % for $Co_3(HXTP)_2$ (X = H, I, T) are 35.29−82.35%, 44.81−96.7%, and 29.57−99.50% in


https://doi.org/10.1021/acsomega.4c10559
ACS Omega 2025, 10, 18380−18390

$Co_3(HXTP)_2$@gas, in Figure 4f, respectively. Furthermore, the adsorption of CO could maximum decrease the values of band gap with the $\Delta E_g$ % changes of 82.35−98.75%. This observation implies that CO adsorption has the most pronounced influence on the conductivity of the $Co_3(HXTP)_2$ material and that CO is the most promising gas for achieving electrochemical gas-sensitive detection. Furthermore, the HOMO and LUMO distributions can reflect the improvement of conductivity. Taking $Co_3(HTTP)_2$@Co as an example, the adsorption of CO introduces a redistribution of electron clouds, causing changes in the energy values of HOMO and LUMO, as depicted in Figure 4g. It is evident that there is a significant quantity of LUMO dispersed around the CO, suggesting that these electrons are free to transfer throughout the adsorption process. Moreover, the HOMO and LUMO band gaps ($E_{L-H}$) significantly reduce upon CO adsorption, thereby enhancing the conductance of the adsorption system and enabling gas detection. The alterations in both the band gaps, HOMO and LUMO orbitals, demonstrate an enhancement in conductivity subsequent to gas adsorption, so $Co_3(HXTP)_2$ can be used as a resistive gas sensor to detect CO, NO, $NO_2$, and $O_2$.

**Sensing Properties and Recovery Time.** Sensing properties are recognized as indicators of the electrochemical gas sensors by considering the change of resistance. The variation of the work function ($\Phi$) can directly reflect the response of the substrate to the gas by changing the resistance of the system. Generally, the $\Phi$ refers to the difference between the vacuum and Fermi levels, as shown in Figure 5a, which is calculated by[50,62−64]

$$\Phi = E_{vac} - E_{Fermi} \tag{6}$$

where the $E_{vac}$ is the vacuum level and the $E_{Fermi}$ is Fermi level. The calculated $\Phi$ (in Table S2) of $Co_3(HHTP)_2$, $Co_3(HITP)_2$, and $Co_3(HTTP)_2$ are 5.302, 4.152, and 5.364 eV, respectively. After the adsorption of GCPs, the $\Phi$ value undergoes considerable changes to the range of 4.063−5.623 eV. The difference of work function ($\Delta\Phi$) between the pristine $Co_3(HXTP)_2$ and the $Co_3(HXTP)_2$@GCPs systems increased with different degrees. For example, the $\Delta\Phi$ of $Co_3(HHTP)_2$@$NO_2/O_2$, $Co_3(HITP)_2$@$NO_2/O_2$, and $Co_3(HTTP)_2$@$NO_2$ are 0.321, 0.129, 0.416, 0.188, and 0.182 eV, respectively, while that of $Co_3(HTTP)_2$@CO is −0.110 eV. Taking $Co_3(HTTP)_2$@CO as an example again, the decrease of the work function implies that electrons can more easily escape from $Co_3(HTTP)_2$, thereby increasing the electron density on the material surface. This indicates that the adsorption process of CO is accompanied by an increase in electrical conductivity, enabling excellent detection of CO by an electrical measurement. So, these pronounced variations in work function demonstrate that the substrate exhibits excellent gas responsiveness and can be preferentially detected. In short, the superior sensing properties of $Co_3(HXTP)_2$ is primarily attributed to the strong chemical interactions. Gas molecules adsorbed within the electron localization cavities of $Co_3(HXTP)_2$ can change the electron transport pathways in the material, resulting in significant changes in its electrical conductivity, which facilitate their detection. In addition, we compared relevant previous studies, as shown in Table 2. It can be seen that our research with a high sensing performance for the adsorption of $NO_2$, $O_2$, and CO demonstrates advantages over some earlier studies. A larger change in the work function indicates a stronger gas-sensing capability, which also suggests

**Table 2. Comparison of the Changes of Work Function ($\Delta\Phi$) of $Co_3(HTTP)_2$@$CO/NO_2/O_2$ in This Study and Previous Studies**

| systems | $\Delta\Phi$, eV | systems | $\Delta\Phi$, eV |
|---|---|---|---|
| $Co_3(HITP)_2$@$NO_2$ (this work) | 0.416 | $Fe_2Pc$@$NO_2$[65] | 0.160 |
| $Co_3(HITP)_2$@$O_2$ (this work) | 0.188 | ZnO-$MoS_2$@$NO_2$[12] | 0.327 |
| $Co_3(HTTP)_2$@CO (this work) | −0.110 | $MoTe_2Sb$@$NO_2$[57] | 0.174 |
| 2D-Mg@CO[45] | 0.001 | Pt-HfTe@$NO_2$[63] | 0.390 |
| Pt-HfTe@CO[63] | 0.110 | b-Bi@CO[66] | 0 |
| SiAs@$O_2$[67] | −0.005 | $C_3N$@$O_2$[68] | 0.190 |

that the $Co_3(HXTP)_2$ material is more suitable for use as a corresponding gas-sensing material. Thus, they are selected for further desorption characteristics studies.

In order to be reused, the adsorbed gas should be able to desorption smoothly so that the gas-sensitive material can return to its preadsorption state; hence, the reasonable recovery time of gas-sensitive materials has been a focus of research. The recovery time ($\tau$) is calculated by[69−71]

$$\tau = A^{-1}\exp\left(\frac{|E_{ads}|}{k_B T}\right) \tag{7}$$

where $E_{ads}$ is the adsorption energy of gases, and the $A^{-1}$ represents the apparent frequency factor ($10^{12}$ $s^{-1}$). The $\tau$ can be reduced by heating, and strong $E_{ads}$ can lead to longer $\tau$, according to the formula. As seen in Figure 5b, the $\tau$ is then investigated at 298 and 498 K. Due to the moderate $E_{ads}$, $Co_3(HHTP)_2$@$O_2$ and $Co_3(HITP)_2$@$O_2$ exhibit rapid recovery at 298 K, with $\tau$ of only 1.226 and 19.441 s, respectively. Furthermore, $Co_3(HTTP)_2$ at 498 K has a short $\tau$ of 694.226 s, indicating that CO can desorb from $Co_3(HTTP)_2$ at high temperatures. However, caused by the large $E_{ads}$, the $\tau$ values for the other systems are significantly prolonged, suggesting their unsuitability as gas-sensitive materials. Therefore, after the adsorption of gases, some $Co_3(HXTP)_2$ can rapidly return to its original surface state within a short period, allowing for the subsequent adsorption, sensing, and desorption of gases. This indicates that it possesses long-term stable gas-sensing performance, significantly enhancing the economic viability of using $Co_3(HXTP)_2$ as a GCPs sensing material. In conclusion, $Co_3(HHTP)_2$@$O_2$, $Co_3(HITP)_2$@$O_2$, and $Co_3(HTTP)_2$@CO exhibit favorable $\tau$ values, demonstrating their suitability as highly efficient gas-sensitive materials.

**Descriptors of the Gas-Sensitive Material.** For gas-sensitive materials, it is essential but challenging to identify key parameters and suitable descriptors. A perfect descriptor should exhibit strong correlation with both the adsorption energies of GCPs ($E_{ads}$) and change in the work function ($\Delta\Phi$). In this regard, we proposed several key parameters and made a heat map of the Pearson correlations related to $E_{ads}$ and $\Delta\Phi$. The features utilized for constructing the Pearson correlation coefficient (P) heat map encompass the electron count in spin-up and spin-down d/p-orbitals ($\alpha$-$Q_{TM\text{-}d}$, $\beta$-$Q_{TM\text{-}d}$, $\alpha$-$Q_{gas\text{-}p}$, $\beta$-$Q_{gas\text{-}p}$) of substate and the GCPs, and electron changes ($\Delta\beta$-$Q_{d_{xz}+d_{yz}}$, $\Delta\beta$-$Q_{d_{z^2}}$) for $d_{xz}$, $d_{yz}$, and $d_{z^2}$ of the Co atom. The LUMO−HOMO band gap ($E_{L-H}$) and average Pauling electronegativity ($\chi_{gas\text{-}average}$) are for the gas molecules. The lattice constant ($a_{slab}$), work function ($\Phi_{slab}$), and d-band center ($\alpha$-$\varphi_d$, $\beta$-$\varphi_d$) for the substrate. In Figure 6a, the chordal thickness connecting each feature represents the


https://doi.org/10.1021/acsomega.4c10559
ACS Omega 2025, 10, 18380−18390

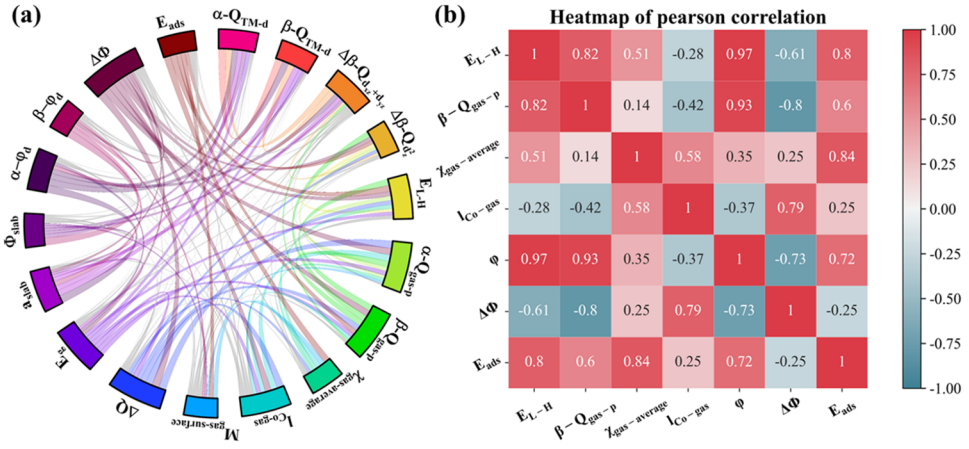


**Figure 6.** (a) Chordal graph of correlations between individual features plotted using Pearson correlations coefficient data, while chordal with lower correlation coefficients are displayed in gray. (b) Heat map of the Pearson correlation coefficient between the $\varphi$, the features used by the constructed descriptor and $\Delta\Phi$, $E_{ads}$.

absolute value of their Pearson correlation coefficient ($P$, detailed parameters can be found in Figure S8). It is noteworthy that some features show strong correlation with either $\Delta\Phi$ or $E_{ads}$, but no feature exhibits an ideal correlation coefficient ($|P| \geq 0.7$) with both targets simultaneously. Thus, we proposed a descriptor $\varphi$ with the following formula:

$$\varphi = \frac{E_{L\text{-}H} \times l_{Co\text{-}gas}}{\beta\text{-}Q_{gas\text{-}p} \times \chi_{gas\text{-}average}} \quad (8)$$

The $\chi_{gas\text{-}average}$ and the $\beta$-$Q_{gas\text{-}p}$ were selected as divisors due to their prevalent use in previous[72−75] descriptors involving the product of electronegativity and electrons count. In this study, incorporating gas properties enables a more comprehensive characterization of diverse adsorption systems compared to focusing solely on the properties of the Co metal. Additionally, these gas-related factors demonstrate a stronger correlation with the target variable, as indicated by the heat map in Figure S8. Meanwhile, the product of $E_{L-H}$ and $l_{Co\text{-}gas}$ was chosen as the dividend, where $E_{L-H}$ exhibits the best dual-correlation performance, and $l_{Co\text{-}gas}$ accounts for the adsorption structure correlation effects. The created descriptor $\varphi$ exhibits an absolute value for the Pearson coefficient of over 0.7 for both $\Delta\Phi$ or $E_{ads}$, as illustrated in Figure 6b. The $\varphi$ exhibit a strong negative correlation coefficient of −0.73 with the work function, and conversely, a significant positive correlation coefficient of 0.72 with the $E_{ads}$. This confirms that it can assess both targets simultaneously. Consequently, we can conclude that descriptor $\varphi$ enables a rapid assessment of the adsorption and response properties of gas-sensitive materials.

## CONCLUSIONS

This study focuses on metal−organic framework structures ($Co_3(HXTP)_2$) to explore their feasibility as gas-sensitive materials for combustion process gases (GCPs). We calculated the adsorption energies ($E_{ads}$), variation in work function ($\Delta\Phi$), and the recovery time ($\tau$) for the adsorption systems. Among these systems, $Co_3(HHTP)_2$@$O_2$, $Co_3(HITP)_2$@$O_2$, and $Co_3(HTTP)_2$@CO exhibit excellent response characteristics with the $\Delta\Phi$ of 0.129 0.188, and −0.110 eV, respectively. For $Co_3(HHTP)_2$@$O_2$ and $Co_3(HITP)_2$@$O_2$, although the adsorption energies are not the best, the moderate $E_{ads}$ (−0.715 and −0.786 eV) imply very short recovery time at 298 K, which are 1.226 and 19.441 s, respectively, suggesting potential in gas-sensitive materials. The $Co_3(HTTP)_2$@CO possesses outstanding $E_{ads}$ of −1.467 eV and $\tau$ of merely 694.226 s at 498 K, which makes $Co_3(HTTP)_2$ a highly promising candidate for CO gas sensing. In the case of $Co_3(HTTP)_2$@CO, the strong chemical interaction follows a "donation−backdonation" mechanism, where electrons transfer between Co and CO ($5\sigma \rightarrow 3d_{z^2}$ and $3d_{xz}$, $3d_{yz} \rightarrow 2\pi^*$), alongside electron rearrangement within d orbitals of Co atom ($3d_{z^2} \rightarrow 3d_{xz}$, $3d_{yz}$). The results of the change in magnetic moment ($\Delta M$), the band gap ($E_g$), and the HOMO and LUMO band gaps ($E_{L-H}$) imply the transfer of electrons and an increase in conductivity. The introduced descriptor $\varphi$ shows a strong linear correlation with $E_{ads}$ and $\Delta\Phi$, with the Pearson correlation coefficient of 0.72 and −0.73, respectively, which can be used as a possible predictor for gas sensitivity. We believe that these findings offer valuable insights for further exploration of $TM_3(HXTP)_2$ as catalysts or gas-sensitive materials.

## ASSOCIATED CONTENT

### Supporting Information

The Supporting Information is available free of charge at https://pubs.acs.org/doi/10.1021/acsomega.4c10559.

Visualizations of charge localization, projected density of states (PDOS), and band structures for $Co_3(HITP)_2$ and $Co_3(HTTP)_2$; PDOS for $Co_3(HHTP)_2$; all considered adsorption configurations along with their corresponding adsorption energy data; total density of states (TDOS) images for the optimized adsorption systems; spin-electron distribution for gas adsorption of $NO_2$, NO, CO, and $O_2$; Pearson correlation coefficient heatmaps containing all relevant data; physical and electronic parameters for the GCP gases and $Co_3(HXTP)_2$ substrate, including bond lengths, bond angles, magnetic moments, HOMO−LUMO gaps of gas molecules and lattice constants, average metal−ligand bond lengths, band gaps, and magnetic moments of the $Co_3(HHTP)_2$ substrate; the average bond lengths of Co-$X_4$ center after gas adsorption and their corresponding changes; adsorption heights of gas molecules; bond lengths of chemical bonds formed between gas molecules and metals; band gaps of gas molecules after



https://doi.org/10.1021/acsomega.4c10559
ACS Omega 2025, 10, 18380−18390

adsorption and their changes; magnetic moments after gas adsorption and their variations; work functions after gas adsorption and their changes; number of electrons transferred between gas molecules and the substrate; and electron counts and changes in $d_{xz}$, $d_{yz}$, and $d_{z^2}$ orbitals for adsorption systems. (PDF)

## AUTHOR INFORMATION


### Corresponding Authors

**Jiezhen Xia** − *State Key Laboratory of Physical Chemistry of Solid Surfaces, iChEM, College of Chemistry and Chemical Engineering, Xiamen University, Xiamen 361005, China*; Email: xia_zangda@163.com

**Qi Wu** − *College of Science, Tibet University, Lhasa 850000, China; Tibet Key Laboratory of Plateau Oxygen and Living Environment, College of Science, Tibet University, Lhasa 850000, China*; orcid.org/0000-0003-2160-6370; Email: wuqi@utibet.edu.cn

### Authors

**Tengrui Feng** − *College of Science, Tibet University, Lhasa 850000, China; Tibet Key Laboratory of Plateau Oxygen and Living Environment, College of Science, Tibet University, Lhasa 850000, China*

**Wanlin Xu** − *College of Science, Tibet University, Lhasa 850000, China; Tibet Key Laboratory of Plateau Oxygen and Living Environment, College of Science, Tibet University, Lhasa 850000, China*

**Degui Lin** − *College of Science, Tibet University, Lhasa 850000, China; Tibet Key Laboratory of Plateau Oxygen and Living Environment, College of Science, Tibet University, Lhasa 850000, China*

Complete contact information is available at: https://pubs.acs.org/10.1021/acsomega.4c10559


### Author Contributions

‖T.F., W.X., and D.L. contributed equally to this work. T.F.: conceptualization, data curation, formal analysis, investigation, methodology, software, visualization, and writing—original draft. W.X.: investigation, methodology, and writing—review and editing. D.L.: investigation, methodology, and writing—review and editing. J.X.: methodology, supervision, validation, and writing—review and editing. Q.W.: resources, supervision, validation, and writing—review and editing.

### Notes

The authors declare no competing financial interest.

## ACKNOWLEDGMENTS

This work was supported by the National Natural Science Foundation of China [Grant No. 22168036]; the Central Government Funds for Local Science and Technological Development [No. XZ202201YD0020C]; the Natural Science Foundation Project of Tibet Autonomous Region [XZ202301ZR0026G]; the Tibet University Graduate High-Level Talent Training Program [Grant No. 2022-GSP-S047]. In addition, we gratefully acknowledge HZWTECH for providing computation facilities.

## REFERENCES


(1) Wang, Z.; Bu, M.; Hu, N.; Zhao, L. An overview on room-temperature chemiresistor gas sensors based on 2D materials: Research status and challenge. *Composites, Part B* **2023**, *248*, No. 110378.

(2) Feng, Q.; Huang, B.; Li, X. Graphene-Based Heterostructure Composite Sensing Materials for Detection of Nitrogen-Containing Harmful Gases. *Adv. Funct. Mater.* **2021**, *31* (41), No. 2104058.

(3) Gao, C.; Zhang, Y.; Yang, H.; Liu, Y.; Liu, Y.; Du, J.; Ye, H.; Zhang, G. A DFT study of In doped Tl2O: a superior NO2 gas sensor with selective adsorption and distinct optical response. *Appl. Surf. Sci.* **2019**, *494*, 162−169.

(4) Liangruksa, M.; Sukpoonprom, P.; Junkaew, A.; Photaram, W.; Siriwong, C. Gas sensing properties of palladium-modified zinc oxide nanofilms: A DFT study. *Appl. Surf. Sci.* **2021**, *544*, No. 148868.

(5) Yang, C.; Yang, Y.; Zhang, C.; Yu, H.; Wang, T.; Shi, K.; Zhang, Z.; Wang, D.; Dong, X. High selectivity of Ag-doped Fe2O3 hollow nanofibers in H2S detection at room operating temperature. *Sens. Actuators, B* **2021**, *341*, No. 129919.

(6) Wu, Y.; Chen, X.; Weng, K.; Arramel; Jiang, J.; Ong, W. J.; Zhang, P.; Zhao, X.; Li, N. Highly Sensitive and Selective Gas Sensor Using Heteroatom Doping Graphdiyne: A DFT Study. *Adv. Electron. Mater.* **2021**, *7* (7), No. 2001244.

(7) Liang, X.-Y.; Ding, N.; Ng, S.-P.; Wu, C.-M. L. Adsorption of gas molecules on Ga-doped graphene and effect of applied electric field: A DFT study. *Appl. Surf. Sci.* **2017**, *411*, 11−17.

(8) Deshpande, S.; Deshpande, M.; Ahuja, R.; Hussain, T. Tuning the electronic, magnetic, and sensing properties of a single atom embedded microporous $C_3N_6$ monolayer towards $XO_2$ (X = C, N, S) gases. *New J. Chem.* **2022**, *46* (28), 13752−13765.

(9) Xiao, Z.; Wu, W.; Wu, X.; Zhang, Y. Adsorption of $NO_2$ on monolayer $MoS_2$ doped with Fe, Co, and Ni, Cu: A computational investigation. *Chem. Phys. Lett.* **2020**, *755*, No. 137768.

(10) Fan, Y.; Zhang, J.; Qiu, Y.; Zhu, J.; Zhang, Y.; Hu, G. A DFT study of transition metal (Fe, Co, Ni, Cu, Ag, Au, Rh, Pd, Pt and Ir)-embedded monolayer $MoS_2$ for gas adsorption. *Comput. Mater. Sci.* **2017**, *138*, 255−266.

(11) Liu, H.; Wang, F.; Hu, K.; Li, T.; Yan, Y.; Li, J. The Adsorption and Sensing Performances of Ir-modified $MoS_2$ Monolayer toward $SF_6$ Decomposition Products: A DFT Study. *Nanomaterials* **2021**, *11* (1), 100.

(12) Wang, M.; Zeng, Q.; Cao, J.; Chen, D.; Zhang, Y.; Liu, J.; Jia, P. Highly Sensitive Gas Sensor for Detection of Air Decomposition Pollutant (CO, NOx): Popular Metal Oxide (ZnO, $TiO_2$)-Doped $MoS_2$ Surface. *ACS Appl. Mater. Interfaces* **2024**, *16* (3), 3674−3684.

(13) Jo, Y. M.; Jo, Y. K.; Lee, J. H.; Jang, H. W.; Hwang, I. S.; Yoo, D. J. MOF-Based Chemiresistive Gas Sensors: Toward New Functionalities. *Adv. Mater.* **2023**, *35* (43), No. 22006842.

(14) Lv, Y.; Xu, P.; Yu, H.; Xu, J.; Li, X. Ni-MOF-74 as sensing material for resonant-gravimetric detection of ppb-level CO. *Sens. Actuators, B* **2018**, *262*, 562−569.

(15) Nguyen, D.-K.; Lee, J.-H.; Nguyen, T.-B.; Le Hoang Doan, T.; Phan, B. T.; Mirzaei, A.; Kim, H. W.; Kim, S. S. Realization of selective CO detection by Ni-incorporated metal-organic frameworks. *Sens. Actuators, B* **2020**, *315*, No. 128110.

(16) Pentyala, V.; Davydovskaya, P.; Ade, M.; Pohle, R.; Urban, G. Carbon dioxide gas detection by open metal site metal organic frameworks and surface functionalized metal organic frameworks. *Sens. Actuators, B* **2016**, *225*, 363−368.

(17) Wu, X.; Xiong, S.; Gong, Y.; Gong, Y.; Wu, W.; Mao, Z.; Liu, Q.; Hu, S.; Long, X. MOF-SMO hybrids as a $H_2S$ sensor with superior sensitivity and selectivity. *Sens. Actuators, B* **2019**, *292*, 32−39.

(18) Sun, L.; Campbell, M. G.; Dincă, M. Electrically Conductive Porous Metal−Organic Frameworks. *Angew. Chem., Int. Ed.* **2016**, *55* (11), 3566−3579.

(19) Ko, M.; Mendecki, L.; Mirica, K. A. Conductive two-dimensional metal−organic frameworks as multifunctional materials. *Chem. Commun.* **2018**, *54* (57), 7873−7891.

(20) Xie, L. S.; Skorupskii, G.; Dincă, M. Electrically Conductive Metal−Organic Frameworks. *Chem. Rev.* **2020**, *120* (16), 8536−8580.

(21) Talin, A. A.; Centrone, A.; Ford, A. C.; Foster, M. E.; Stavila, V.; Haney, P.; Kinney, R. A.; Szalai, V.; Gabaly, F. E.; Yoon, H. P.;

et al. Reticular synthesis and the design of new materials. *Science* **2014**, *423* (6941), 705−714.
(22) Downes, C. A.; Clough, A. J.; Chen, K.; Yoo, J. W.; Marinescu, S. C. Evaluation of the H2 Evolving Activity of Benzenehexathiolate Coordination Frameworks and the Effect of Film Thickness on $H_2$ Production. *ACS Appl. Mater. Interfaces* **2018**, *10* (2), 1719−1727.
(23) Mendecki, L.; Mirica, K. A. Conductive Metal−Organic Frameworks as Ion-to-Electron Transducers in Potentiometric Sensors. *ACS Appl. Mater. Interfaces* **2018**, *10* (22), 19248−19257.
(24) Li, J.; Huang, Y.; Zhou, Y.; Dong, H.; Wang, H.; Shan, H.; Li, Y.; Xu, M.; Wang, X. Controllable Construction of Two-Dimensional Conductive $M_3(HHTP)_2$ Nanorods for Electrochemical Sensing of Malachite Green in Fish. *ACS Appl. Nano Mater.* **2023**, *6* (24), 22916−22926.
(25) Mähringer, A.; Jakowetz, A. C.; Rotter, J. M.; Bohn, B. J.; Stolarczyk, J. K.; Feldmann, J.; Bein, T.; Medina, D. D. Oriented Thin Films of Electroactive Triphenylene Catecholate-Based Two-Dimensional Metal−Organic Frameworks. *ACS Nano* **2019**, *13* (6), 6711−6719.
(26) Campbell, M. G.; Sheberla, D.; Liu, S. F.; Swager, T. M.; Dincă, M. $Cu_3$(hexaiminotriphenylene)$_2$: An Electrically Conductive 2D Metal−Organic Framework for Chemiresistive Sensing. *Angew. Chem., Int. Ed.* **2015**, *54* (14), 4349−4352.
(27) Lian, Y.; Yang, W.; Zhang, C.; Sun, H.; Deng, Z.; Xu, W.; Song, L.; Ouyang, Z.; Wang, Z.; Guo, J.; Peng, Y. Unpaired 3d Electrons on Atomically Dispersed Cobalt Centres in Coordination Polymers Regulate both Oxygen Reduction Reaction (ORR) Activity and Selectivity for Use in Zinc−Air Batteries. *Angew. Chem., Int. Ed.* **2020**, *59* (1), 286−294.
(28) Yao, M. S.; Lv, X. J.; Fu, Z. H.; Li, W. H.; Deng, W. H.; Wu, G. D.; Xu, G. Layer-by-Layer Assembled Conductive Metal−Organic Framework Nanofilms for Room-Temperature Chemiresistive Sensing. *Angew. Chem., Int. Ed.* **2017**, *56* (52), 16510−16514.
(29) Hmadeh, M.; Lu, Z.; Liu, Z.; Gándara, F.; Furukawa, H.; Wan, S.; Augustyn, V.; Chang, R.; Liao, L.; Zhou, F.; et al. New Porous Crystals of Extended Metal-Catecholates. *Chem. Mater.* **2012**, *24* (18), 3511−3513.
(30) Miner, E. M.; Wang, L.; Dincă, M. Modular $O_2$ electroreduction activity in triphenylene-based metal−organic frameworks. *Chem. Sci.* **2018**, *9* (29), 6286−6291.
(31) Clough, A. J.; Skelton, J. M.; Downes, C. A.; de la Rosa, A. A.; Yoo, J. W.; Walsh, A.; Melot, B. C.; Marinescu, S. C. Metallic Conductivity in a Two-Dimensional Cobalt Dithiolene Metal−Organic Framework. *J. Am. Chem. Soc.* **2017**, *139* (31), 10863−10867.
(32) Sheberla, D.; Sun, L.; Blood-Forsythe, M. A.; Er, S.; Wade, C. R.; Brozek, C. K.; Aspuru-Guzik, A.; Dincă, M. High Electrical Conductivity in $Ni_3$(2,3,6,7,10,11-hexaiminotriphenylene)$_2$, a Semiconducting Metal−Organic Graphene Analogue. *J. Am. Chem. Soc.* **2014**, *136* (25), 8859−8862.
(33) Wu, X.; Xu, W.; Wang, Z.; Li, H.; Wang, M.; Zhang, D.; Lai, J.; Wang, L. Rapid microwave synthesis of Ru-supported partially carbonized conductive metal−organic framework for efficient hydrogen evolution. *Chem. Eng. J.* **2022**, *431*, No. 133247.
(34) Wang, J.; Li, F.; Liu, Z.; Dai, Z.; Gao, S.; Zhao, M. Two-Dimensional Conductive Metal−Organic Frameworks as Highly Efficient Electrocatalysts for Lithium−Sulfur Batteries. *ACS Appl. Mater. Interfaces* **2021**, *13* (51), 61205−61214.
(35) Tian, Y.; Zhao, T.; Zhao, C.; Likai, Y. Two−dimensional metal organic nanosheet as promising electrocatalysts for carbon dioxide reduction: A computational study. *Appl. Surf. Sci.* **2022**, *597*, No. 153724.
(36) Momeni, M. R.; Zhang, Z.; Dell'Angelo, D.; Shakib, F. A. Tuning electronic properties of conductive 2D layered metal−organic frameworks via host−guest interactions: Dioxygen as an electroactive chemical stimuli. *APL Mater.* **2021**, *9* (5), No. 051109.
(37) Campbell, M. G.; Liu, S. F.; Swager, T. M.; Dincă, M. Chemiresistive Sensor Arrays from Conductive 2D Metal−Organic Frameworks. *J. Am. Chem. Soc.* **2015**, *137* (43), 13780−13783.
(38) Bhauriyal, P.; Heine, T. Catalysing the performance of Li−sulfur batteries with two-dimensional conductive metal organic frameworks. *J. Mater. Chem. A* **2022**, *10* (23), 12400−12408.
(39) Hafner, J. Ab-initiosimulations of materials using VASP: Density-functional theory and beyond. *J. Comput. Chem.* **2008**, *29* (13), 2044−2078.
(40) Blöchl, P. E. Projector augmented-wave method. *Phys. Rev. B* **1994**, *50* (24), 17953−17979.
(41) Perdew, J. P.; Yue, W. Accurate and simple density functional for the electronic exchange energy: Generalized gradient approximation. *Phys. Rev. B* **1986**, *33* (12), 8800−8802.
(42) Grimme, S.; Antony, J.; Ehrlich, S.; Krieg, H. A consistent and accurate ab initio parametrization of density functional dispersion correction (DFT-D) for the 94 elements H-Pu. *J. Chem. Phys.* **2010**, *132*, No. 154104.
(43) Cheng, Z.; Zhang, X.; Zhang, H.; Liu, H.; Yu, X.; Dai, X.; Liu, G.; Chen, G. $BeN_4$ monolayer as an excellent Dirac anode material for potassium-ion batteries. *J. Alloys Compd.* **2023**, *936*, No. 168351.
(44) Toton, D.; Lorenz, C. D.; Rompotis, N.; Martsinovich, N.; Kantorovich, L. Temperature control in molecular dynamic simulations of non-equilibrium processes. *J. Phys.: Condens. Matter* **2010**, *22* (7), No. 074205.
(45) Thomas, S.; Mayr, F.; Madam, A. K.; Gagliardi, A. Machine learning and DFT investigation of CO, $CO_2$and $CH_4$ adsorption on pristine and defective two-dimensional magnesene. *Phys. Chem. Chem. Phys.* **2023**, *25* (18), 13170−13182.
(46) Zhao, P.; Tang, M.; Zhang, D. Adsorption of dissolved gas molecules in the transformer oil on metal (Ag, Rh, Sb)-doped $PdSe_2$ momlayer: A first-principles study. *Appl. Surf. Sci.* **2022**, *600*, No. 154054.
(47) Du, R.; Wu, W. Adsorption of gas molecule on Rh, Ru doped monolayer $MoS_2$ for gas sensing applications: A DFT study. *Chem. Phys. Lett.* **2022**, *789*, No. 139300.
(48) Aghaei, S. M.; Monshi, M. M.; Torres, I.; Zeidi, S. M. J.; Calizo, I. DFT study of adsorption behavior of NO, CO, $NO_2$, and $NH_3$ molecules on graphene-like $BC_3$: A search for highly sensitive molecular sensor. *Appl. Surf. Sci.* **2018**, *427*, 326−333.
(49) Isa, M.; Ashfaq, I.; Majid, A.; Shakil, M.; Iqbal, T. A DFT study of silver decorated bismuthene for gas sensing properties and effect of humidity. *Mater. Sci. Semicond. Process.* **2022**, *145*, No. 106635.
(50) Kumar, V.; Rajput, K.; Roy, D. R. Sensing applications of GeBi nanosheet for environmentally toxic/non-toxic gases: Insights from density functional theory calculations. *Appl. Surf. Sci.* **2022**, *606*, No. 154741.
(51) Yu, Y.; Dai, C. DFT study of gas adsorption and sensing based on noble metal (Ag, Au and Pt) functionalized boron selenide nanosheets. *Physica E* **2021**, *125*, No. 114409.
(52) Wang, D.; She, A.; Yang, H.; Liu, X.; Li, H.; Feng, M. $Fe_2GeS_4$ (010) surface oxidation mechanism and potential application of the oxidized surface in gas sensing: A first-principles study. *J. Alloys Compd.* **2021**, *888*, No. 161532.
(53) Kumar, V.; Jung, J. Enhancement of gas sensing by doping of transition metal in two-dimensional $As_2C_3$ nanosheet: A density functional theory investigation. *Appl. Surf. Sci.* **2022**, *599*, No. 153941.
(54) Chepkasov, I. V.; Sukhanova, E. V.; Kvashnin, A. G.; Zakaryan, H. A.; Aghamalyan, M. A.; Mamasakhlisov, Y. S.; Manakhov, A. M.; Popov, Z. I.; Kvashnin, D. G. Computational Design of Gas Sensors Based on $V_3S_4$ Monolayer. *Nanomaterials* **2022**, *12* (5), 774.
(55) Sun, X.; Song, Z.; Liu, Q.; Xiao, B.; Li, Y.; Cheng, J.; Liu, Z.; Yang, X.; Yu, X.; Li, Q. First-principles study on the C-excess $C_3B$ for its potential application in sensing $NO_2$ and NO. *Appl. Surf. Sci.* **2020**, *512*, No. 145611.
(56) Dai, J.; Yuan, J. Adsorption of molecular oxygen on doped graphene: Atomic, electronic, and magnetic properties. *Phys. Rev. B* **2010**, *81* (16), No. 165414.
(57) Panigrahi, P.; Hussain, T.; Karton, A.; Ahuja, R. Elemental Substitution of Two-Dimensional Transition Metal Dichalcogenides ($MoSe_2$and $MoTe_2$): Implications for Enhanced Gas Sensing. *ACS Sens.* **2019**, *4* (10), 2646−2653.


https://doi.org/10.1021/acsomega.4c10559
*ACS Omega* 2025, 10, 18380−18390

(58) Sakhuja, N.; Jha, R. K.; Chaurasiya, R.; Dixit, A.; Bhat, N. 1T-Phase Titanium Disulfide Nanosheets for Sensing $H_2S$ and $O_2$. *ACS Appl. Nano Mater.* **2020**, *3* (4), 3382−3394.
(59) Zhang, Y.; Wang, Y.; Ma, N.; Li, Y.; Liang, B.; Luo, S.; Fan, J. Establishing an orbital-level understanding of active origins of heteroatom-coordinated single-atom catalysts: The case of $N_2$ reduction. *J. Colloid Interface Sci.* **2023**, *650*, 961−971.
(60) Khan, M. I.; Hassan, M.; Majid, A.; Shakil, M.; Rafique, M. DFT perspective of gas sensing properties of Fe-decorated monolayer antimonene. *Appl. Surf. Sci.* **2023**, *616*, No. 156520.
(61) Chen, D.; Zhang, X.; Tang, J.; Cui, Z.; Cui, H. Pristine and Cu decorated hexagonal InN monolayer, a promising candidate to detect and scavenge $SF_6$ decompositions based on first-principle study. *J. Hazard. Mater.* **2019**, *363*, 346−357.
(62) Raval, D.; Gupta, S. K.; Gajjar, P. N. Detection of $H_2S$, HF and $H_2$ pollutant gases on the surface of penta-$PdAs_2$ monolayer using DFT approach. *Sci. Rep.* **2023**, *13* (1), No. 699.
(63) Hu, J.; Zhai, S.; Zhang, Q.; Cui, H.; Jiang, X. Two-dimensional $HfTe_2$ monolayer treated by dispersed single Pt atom for hazardous gas Detection: A First-principles study. *Appl. Surf. Sci.* **2022**, *605*, No. 154572.
(64) Guo, G.; Mao, L.; Liu, K.; Tan, X. Pd-Adsorbed $SiN_3$ Monolayer as a Promising Gas Scavenger for $SF_6$ Partial Discharge Decomposition Components: Insights from the First-Principles Study. *Langmuir* **2024**, *40* (14), 7669−7679.
(65) Ma, Y.; Xiong, H.; Gan, L.; Deng, G. Theoretical investigation of FeMnPc, $Fe_2Pc$, $Mn_2Pc$ monolayers as a potential gas sensors for nitrogenous toxic gases. *Surf. Interfaces* **2024**, *45*, No. 103910.
(66) Pan, W.; Qi, N.; Zhao, B.; Chang, S.; Ye, S.; Chen, Z. Gas sensing properties of buckled bismuthene predicted by first-principles calculations. *Phys. Chem. Chem. Phys.* **2019**, *21* (21), 11455−11463.
(67) Zhao, J.; Cui, X.; Huang, Q.; Zeng, H. Adsorption behavior of small molecule on monolayered SiAs and sensing application for $NO_2$ toxic gas. *Appl. Surf. Sci.* **2023**, *613*, No. 156010.
(68) Zhao, Z.; Yong, Y.; Hu, S.; Li, C.; Kuang, Y. Adsorption of gas molecules on a $C_3N$ monolayer and the implications for $NO_2$ sensors. *AIP Adv.* **2019**, *9* (12), No. 125308.
(69) Tang, H.; Xiang, Y.; Zhan, H.; Zhou, Y.; Kang, J. DFT investigation of transition metal-doped graphene for the adsorption of HCl gas. *Diam. Relat. Mater.* **2023**, *136*, No. 109995.
(70) Li, Y.; Meng, Y.; Li, X.; Sun, J.; Li, X. $FeN_4$-embedded warped nanographene as a potential candidate for scavenging and detecting sulfur-based gases: A DFT study. *J. Environ. Chem. Eng.* **2023**, *11* (3), No. 109705.
(71) Ma, D.; Zhang, J.; Li, X.; He, C.; Lu, Z.; Lu, Z.; Yang, Z.; Wang, Y. $C_3N$ monolayers as promising candidates for $NO_2$ sensors. *Sens. Actuators, B* **2018**, *266*, 664−673.
(72) Gao, S.; Cheng, Y.; Chen, L.; Huang, S. Rapid Discovery of Gas Response in Materials Via Density Functional Theory and Machine Learning. *Energy Environ. Mater.* **2024**, *0*, No. e12816.
(73) Xu, H.; Cheng, D.; Cao, D.; Zeng, X. Revisiting the universal principle for the rational design of single-atom electrocatalysts. *Nat. Catal.* **2024**, *7*, 207−218.
(74) Qi, L.; Gao, W.; Jiang, Q. Effective Descriptor for Designing High-Performance Catalysts for the Hydrogen Evolution Reaction. *J. Phys. Chem. C* **2020**, *124* (42), 23134−23142.
(75) Xu, R.; Bo, T.; Cao, S.; Mu, N.; Liu, Y.; Chen, M.; Zhou, W. High-throughput screening of transition metal doping and defect engineering on single layer $SnS_2$ for the water splitting hydrogen evolution reaction. *J. Mater. Chem. A* **2022**, *10* (40), 21315−21326.


https://doi.org/10.1021/acsomega.4c10559
*ACS Omega* 2025, 10, 18380−18390